PNAS RESEARCH ARTICLE | BIOPHYSICS AND COMPUTATIONAL BIOLOGY

Multiple retinal isomerizations during the early phase of the bestrhodopsin photoreaction

Spyridon Kaziannis[a,b,1], Matthias Broser[c,1], Ivo H. M. van Stokkum[d], Jakub Dostal[a], Wayne Busse[c], Arno Munhoven[c], Cesar Bernardo[a], Miroslav Kloz[a], Peter Hegemann[c,2], and John T. M. Kennis[d,2]

Contributed by Peter Hegemann; received November 1, 2023; accepted February 13, 2024; reviewed by Samer Gozem, Masashi Unno, and Josef Wachtveitl

Bestrhodopsins constitute a class of light-regulated pentameric ion channels that consist of one or two rhodopsins in tandem fused with bestrophin ion channel domains. Here, we report on the isomerization dynamics in the rhodopsin tandem domains of *Phaeocystis antarctica* bestrhodopsin, which binds all-trans retinal Schiff-base (RSB) absorbing at 661 nm and, upon illumination, converts to the meta-stable P540 state with an unusual 11-*cis* RSB. The primary photoproduct P682 corresponds to a mixture of highly distorted 11-*cis* and 13-*cis* RSB directly formed from the excited state in 1.4 ps. P673 evolves from P682 in 500 ps and contains highly distorted 13-*cis* RSB, indicating that the 11-*cis* fraction in P682 converts to 13-*cis*. Next, P673 establishes an equilibrium with P595 in 1.2 µs, during which RSB converts to 11-*cis* and then further proceeds to P560 in 48 µs and P540 in 1.0 ms while remaining 11-*cis*. Hence, extensive isomeric switching occurs on the early ground state potential energy surface (PES) on the hundreds of ps to µs timescale before finally settling on a metastable 11-*cis* photoproduct. We propose that P682 and P673 are trapped high up on the ground-state PES after passing through either of two closely located conical intersections that result in 11-*cis* and 13-*cis* RSB. Co-rotation of C11=C12 and C13=C14 bonds results in a constricted conformational landscape that allows thermal switching between 11-*cis* and 13-*cis* species of highly strained RSB chromophores. Protein relaxation may release RSB strain, allowing it to evolve to a stable 11-*cis* isomeric configuration in microseconds.

far-red absorbing rhodopsin | multiple retinal isomerization | femtosecond to millisecond spectroscopy | femtosecond stimulated Raman spectroscopy | conical intersection

Significance

The far-red absorbing rhodopsin modules (λ_{max} = 661 nm) of bestrhodopsin are of high interest for a principle understanding of the photophysics and photochemistry of unusually far-red absorbing rhodopsins and optogenetic application in tissues that are more transparent to red light in comparison to blue or green light. Moreover, the identified light-induced isomeric switching processes on the ground state potential energy surface disclose a multi-isomerization activation mechanism that has so far remained unknown for rhodopsin.

Microbial rhodopsins are photoactivatable retinal binding membrane proteins (1, 2) that have a significant impact as modulating tools in optogenetics (2, 3) and voltage sensing (4). In most cases, microbial rhodopsins act as standalone pumps or channels that, when light-activated, actively or passively transport ions across the membrane through a pore or ion transfer pathway within the 7-membrane helical structure (1). However, enzymerhodopsins (5, 6) and sensory rhodopsins (1) are exceptions, and their enzymatic or signaling domains are instead regulated by a rhodopsin domain.

Bestrhodopsins have recently been discovered in a number of marine microalgae, including chlorophytes, haptophytes, and dinoflagellates, all consisting of one rhodopsin or two fused rhodopsins in tandem and a bestrophin domain (R-B and RR-B), forming gigantic pentameric structures with 5 or 10 rhodopsin modules (7). Bestrophins are ubiquitous in a number of kingdoms of life, where they serve as chloride-permeant anion channels in mammals and plants, with significant permeability of carbonate anions (8, 9). The bestrhodopsin function is unknown, but in *Chlamydomonas,* bestrophin channels are involved in CO_2 concentrating mechanisms into the lumen of the chloroplast envelope, transporting carbonate anions (10, 11). The recently discovered bestrhodopsin of *Karlodinium veneficum* (Kv-RRB) has been demonstrated to act as a light-modulated chloride channel when expressed in mammalian cells (7).

Bestrhodopsins bind an all-*trans* retinal Schiff base (RSB) chromophore, and most of them are expected to have an unusually red-shifted absorption spectrum peaking near 660 nm (7). Recently, a great interest in red-shifted microbial rhodopsins has arisen, in particular with the discoveries of fungal Neorhodopsins (12–14) and Chrimson (15, 16) because red or near-infrared light penetrates deeper in mammalian brain tissues (17) and potential opportunities for dual color applications (18, 19). Another unusual property of bestrhodopsin concerns its photochemistry, which involves an all-*trans* to *11-cis* RSB isomerization (7) rather than the all-*trans* to *13-cis* photoreaction of canonical microbial rhodopsins (1). In bacteriorhodopsin, all-*trans* to 13-*cis* isomerization was first proposed by resonance Raman studies (20, 21) and further demonstrated by cryo-trapped and

Author affiliations: [a]The Extreme Light Infrastructure ERIC, Dolní Břežany 252 41, Czech Republic; [b]Department of Physics, University of Ioannina, Ioannina Gr-45110, Greece; [c]Faculty of Life Sciences, Institute for Biology, Experimental Biophysics, Humboldt-Universität zu Berlin, Berlin D-10115, Germany; and [d]Department of Physics and Astronomy, Faculty of Science, Vrije Universiteit Amsterdam, Amsterdam 1081 HV, The Netherlands

Author contributions: J.D., M.K., P.H., and J.T.M.K. designed research; S.K., M.B., J.D., W.B., A.M., C.B., and M.K. performed research; J.D. contributed new reagents/analytic tools; S.K., M.B., I.H.M.v.S., C.B., M.K., P.H., and J.T.M.K. analyzed data; and I.H.M.v.S., P.H., and J.T.M.K. wrote the paper.

Reviewers: S.G., Georgia State University; M.U., Saga Daigaku; and J.W., Goethe University Frankfurt.

The authors declare no competing interest.

[1]S.K. and M.B. contributed equally to this work.

[2]To whom correspondence may be addressed. Email: hegemann@rz.hu-berlin.de or j.t.m.kennis@vu.nl.

This article contains supporting information online at https://www.pnas.org/lookup/suppl/doi:10.1073/pnas.2318996121/-/DCSupplemental.

Published March 13, 2024.

transient X-ray structures (22–24). Many questions have since emerged about the nature of bestrhodopsin's far-red absorption, the effect on its photochemistry, and how the *11-cis* products are formed and favored over *13-cis*.

Femtosecond stimulated Raman spectroscopy (FSRS) is a powerful method to gain detailed molecular information on photosensory protein reaction dynamics through recording of transient vibrational spectra (25). It features a high temporal resolution of <100 fs, high spectral resolution and a high signal-to-noise ratio. We have developed an FSRS method involving shot-to-shot Raman pump modulation to successfully suppress large and unpredictable baseline fluctuations and increase signal quality (26–30). Here, we study the photoreaction dynamics of bestrhodopsin from *Phaeocystis antarctica* with femtosecond to sub-millisecond transient absorption (TA) (31, 32), flash photolysis, and FSRS (26, 33) spectroscopy, disentangling the highly complex bestrhodopsin photoreaction in considerable detail.

Results and Discussion

Steady-State Stimulated Raman Spectroscopy. We used the detergent-purified R1/R2 tandem of *P. antarctica* bestrhodopsin (PaR1R2) to follow the photoreaction dynamics. Steady-state absorption of the dark-adapted PaR1R2 peaks at 661 nm (D661; Fig. 1*C*) and can be photoconverted into a metastable green-absorbing state P540, which remains stable in darkness for several tens of minutes at room temperature. To assess the RSB structure of the (metastable) static states, we performed steady-state stimulated Raman spectroscopy in the dark and under continuous illumination. D661 was accumulated either by green background illumination or through extended dark adaptation, which resulted in essentially identical Raman spectra (*SI Appendix*, Fig. S1). Stimulated Raman excitation using wavelength-modulated narrowband pulses of picosecond duration was set at 800 nm (29, 32, 33), which implies a pre-resonance with both the D661 and P540 states. Stimulated Raman spectroscopy provided results comparable to those of (pre)resonance Raman spectroscopy but features rapid data collection and is insensitive to sample fluorescence (26, 32–35).

The Fig. 2 shows the stimulated Raman spectrum of D661 (red line), along with the all-*trans* RSB structure and atom numbering. The overall band pattern is similar to other microbial rhodopsins with a major C=C ethylenic stretch vibrational band located at 1,494 cm^{-1}, which is at a lower frequency than any other native rhodopsin, consistent with an absorption maximum in the far red (34, 36), and in close agreement with Fourier-Transform Infrared Spectroscopy (FTIR) results on Tara-RRB (7), a bestrhodopsin closely related to *P. antarctica*. D661 shows a dominant C-C stretch mode in the fingerprint region at 1,165 cm^{-1} and a significant hydrogen-out-of-plane (HOOP) mode at 952 cm^{-1}. These signatures differ significantly from the light-adapted resting state of bacteriorhodopsin, which shows two C-C bands at 1,165 and 1,201 cm^{-1} at equal intensities and low HOOP intensities (20). Instead, the D661 Raman spectrum is similar to the BR O intermediate (37), which features a distorted all-*trans* RSB, an absorption maximum in the red, and a protonated counterion.

The origin and character of RSB HOOP modes are briefly described in *SI Appendix, Supporting Text*. The bestrhodopsin 952 cm^{-1} band can be assigned to the C11H=C12H A_u HOOP mode (38), which indicates that the RSB is significantly twisted specifically about the C11=C12 bond. In addition, D661 features two small bands at 1,563 and 1,587 cm^{-1}, likely C=C modes involving C13=C14 (38) and a $C=NH^+$ stretch around 1,635 cm^{-1}, similar to bacteriorhodopsin. We further note the presence of the methyl rock vibration at 1,003 cm^{-1}, which involves the coupled vibrations of C19 and C20 methyl groups substituted on the polyene backbone (38, 39). Hence, we conclude that the RSB assumes an all-*trans* configuration in D661 consistent with the cryo-EM structure and HPLC analysis of retinal in Tara-RRB. A protonated nearest counterion (7) and a structurally distorted RSB result in a more delocalized π-electron system, jointly contributing to a red-shifted absorption. Indeed, increasing the pH in Tara-RRB

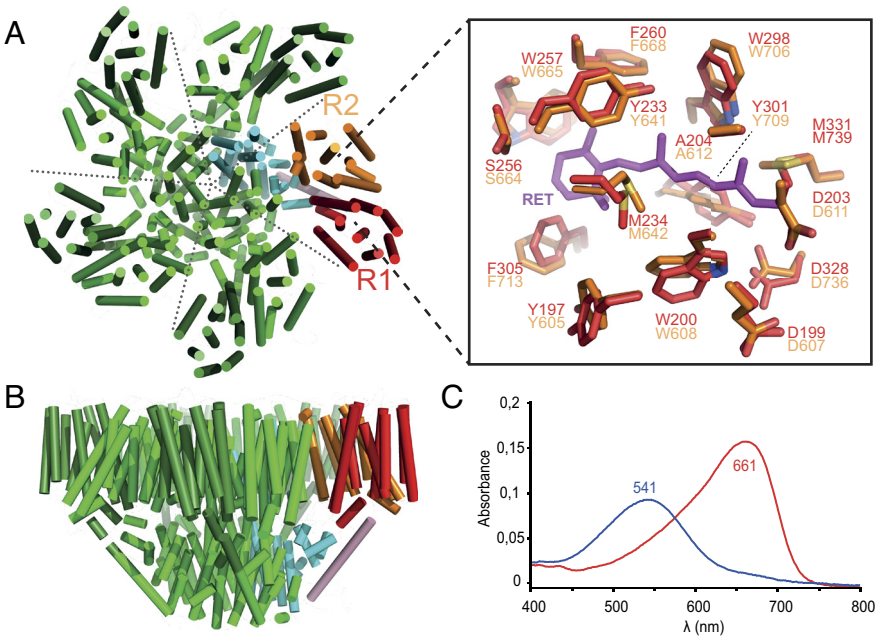

Fig. 1. Bestrhodopsin from *P. antarctica*. (*A*) Homology model (based (7PL9) (7) of pentameric Bestrhodopsin (PaR1R2-B) assembly with one monomer marked: Rhodopsin 1 (R1, red); Rhodopsin 2 (R2, orange); helix connecting R1/R2 (violet); Bestrophin (cyan). The dotted lines demarcate the units in the pentameric structure. Box: Superimposed retinal binding pocket (R1, red; R2, orange) (*B*) side view (*C*) Absorption of purified PaR1R2 in red-state D661 (red line) and metastable green-state P540 (blue line).

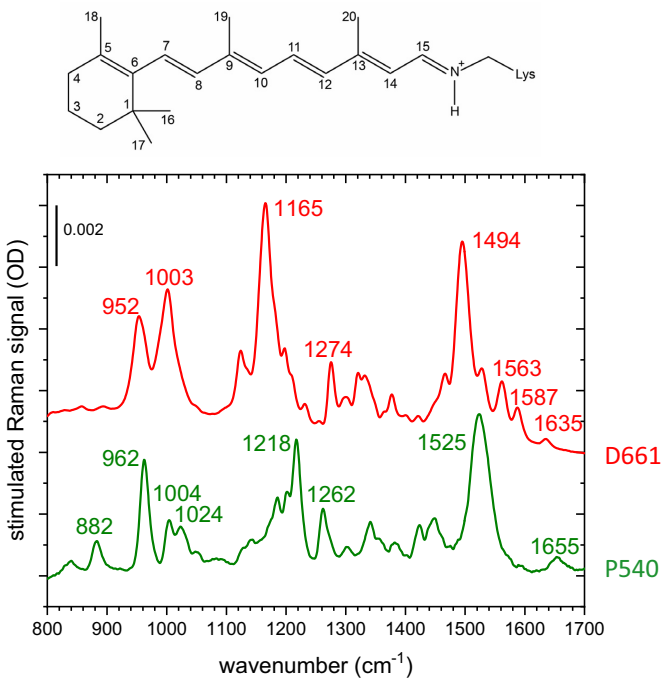

Fig. 2. RSB structure and steady-state stimulated Raman spectra of bestrhodopsin. (*Upper*) all-*trans* RSB structure and atom numbering. (*Lower*) Stimulated Raman spectra of D661 (red line) and P540 (green line) in steady-state upon Raman excitation at 800 nm.

bestrhodopsin leads to a significant blue shift of the absorption to 560 nm, indicative of counterion deprotonation (7).

The Fig. 2 also shows the steady-state stimulated Raman spectrum of P540 (green line) photoaccumulated through background illumination with red light. The P540 Raman spectrum shows a C=C ethylenic vibrational stretch mode at 1,525 cm^{-1}, consistent with an absorption maximum near 540 nm (36). Strikingly, it exhibits a notable C-C stretch vibrational band at 1,218 cm^{-1} at the same frequency as in FTIR for Tara-RRB, where it was assigned to 11-*cis* RSB (7). Furthermore, the P540 Raman spectrum exhibits significant HOOP intensity at 962 cm^{-1} assigned to the C11H=C12H A_u mode (40), which is indicative of a distortion around the C11=C12 *cis* bond. The weak 838 cm^{-1} band is likely due to the C10H HOOP (40), whereas the origin of the 882 cm^{-1} mode is unclear. Notably, the methyl rock vibration of the 11-*cis* RSB of P540 has been split into two bands at 1,004 and 1,024 cm^{-1}. This splitting results from degeneracy lifting upon 11-*cis* isomerization, bringing the two methyls to opposite sides of the C11=C12 double bond (39). Hence, we conclude that the P540 Raman signature is consistent with an 11-*cis* RSB isomeric conformer distorted around the C11=C12 double bond. The band at 1,655 cm^{-1} likely corresponds to protein Amide I modes.

TA Spectroscopy. To assess the reaction dynamics of bestrhodopsin, we performed femtosecond–submillisecond TA spectroscopy (41) utilizing electronically synchronized Ti:sapphire laser systems (26, 31, 32). The results are presented as a global analysis (42). Fig. 3*A* shows the results of a sequential analysis as evolution-associated difference spectra (EADS). In a sequential analysis, the system evolves from state 1 → 2 → 3 →, etc. with increasing exponential rate constants, and the EADS correspond to the spectra of these sequential intermediates. *SI Appendix*, Fig. S2 shows the raw data and fitted kinetics. Seven components were required for an adequate fit of the data, with time constants of 1.4 ps, 11 ps, 32 ps, 500 ps, 1.2 µs, 48 µs, and a nondecaying component. In general, excited-state TA difference spectra consist of a superposition of ground-state bleach (GSB), stimulated emission (SE), and excited-state absorption (ESA) (41). We observe a highly multiexponential excited-state decay, with the first three EADS [1.4 ps (gray line), 11 ps (orange line), and 32 ps (cyan line)], showing GSB at 660 nm, SE at 800 nm, and ESA at 480 nm. Here, the 1.4 ps component shows a minor amplitude (gray to orange line evolution), while the 11 ps component carries the largest part of the decay amplitude (orange to cyan line evolution). The bestrhodopsin excited-state lifetimes are similar to those of the bacteriorhodopsin D85S mutant (43, 44), which may be regarded as a model system for the bacteriorhodopsin O intermediate (45). Similarly long multiexponential excited-state lifetimes were reported for other microbial rhodopsins with neutral counterions (46, 47).

After the decay of the excited state, a primary photoproduct at low amplitude was observed with a maximum in the difference spectrum at 730 nm (dark green line), which evolves in 500 ps to a secondary product with a difference spectrum maximum at 700 nm (black line). In turn, this species evolved into a third product with a maximum at 590 nm (red line) in 1.2 µs, which subsequently evolved to a 4th product with a maximum at 560 nm (blue line) in 48 µs. Note that the EADS of the product states in Fig. 3*A* were expanded ten times. The EADS of the early products had a GSB at a very low amplitude, indicating that extensive compensation of the GSB by product absorption occurs. Fig. 3*B* shows the results of a flash photolysis experiment, which reports on the absorbance difference of the sample upon application a nanosecond flash and complements the µs–s time regime to identify late photoproducts. Global fitting of the data using the same lifetimes as the ultrafast experiment reproduced the spectral signature of the 2nd, 3rd, and 4th products (black, red, and blue lines, respectively). In addition, we resolved a spectral evolution in 1.0 ms to the final state, which involved a blue-shift to the fifth product (magenta line). The latter state coincides with the difference spectrum of steady-state P540 minus D661 and may be regarded as P540.

To identify the absolute spectra of the photointermediates devoid of the GSB component and to quantitatively estimate the product quantum yield, we performed a target analysis (48). The resulting species-associated spectra (SAS) are shown in Fig. 3 *C* and *D*, and details are given in *SI Appendix, Supporting Text*. In short, we could describe the photodynamics in the photocycle model, as depicted in Fig. 4, with products P682, P673, P595, P560, and P540, which interconvert on the timescales of 500 ps, 1.2 µs, 48 µs, and 1 ms, respectively. P673 and P595 exist in a 1:1 equilibrium with a time constant of 1.2 µs. The SAS in Fig. 3*C* were estimated using a quantum yield of 11% (as explained in *SI Appendix*, Fig. S3). The P682 and P673 SAS show a spike at 680 nm, which results from an artifact of unknown origin in the TA data, which we will not discuss further. Inspection of the corresponding SADS (*SI Appendix*, Fig. S3*E*) reveals that the spike is present there as well.

To check whether the complexity of the bestrhodopsin photocycle might be related to the presence of two RSBs in the tandem construct, we constructed a mutant (PaR1(K332A)R2) where the conserved lysine of rhodopsin domain R1 was replaced by alanine, resulting in a construct that binds only a single RSB at rhodopsin domain R2. We performed TA spectroscopy on the PaR1(K332A) R2 mutant, and the EADS that follow from a sequential analysis are shown in *SI Appendix*, Fig. S4*A*. The excited state decayed with 1.0 ps, 9 ps, and 35 ps, while the products evolved with time constants of 380 ps, 1.3 µs, and 38 µs, similar to those of wild type. We then analyzed the data in a scheme and with rate

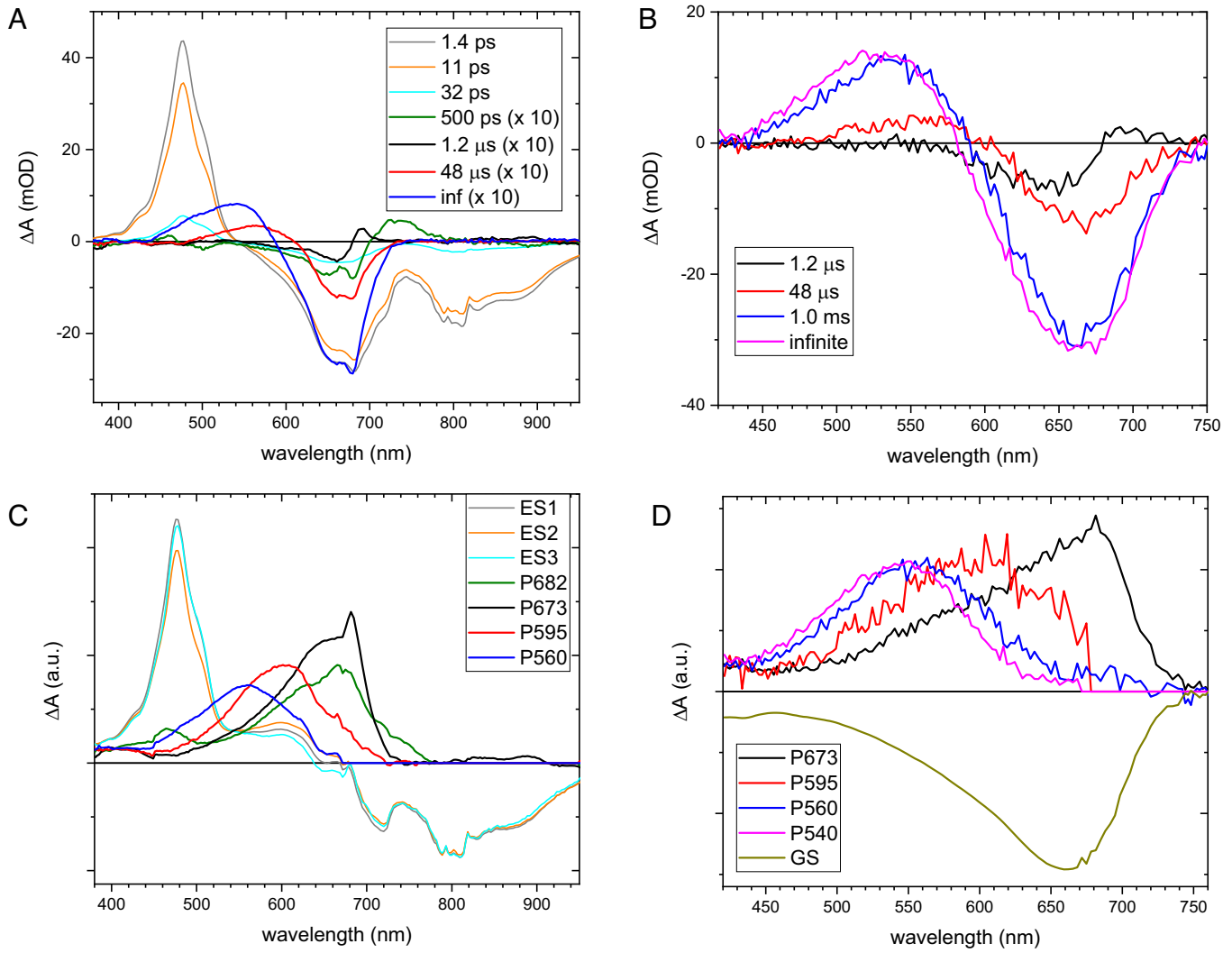

Fig. 3. Time-resolved spectroscopy of bestrhodopsin. (*A*) fs – sub-ms TA spectroscopy, EADS resulting from a sequential analysis with time constants indicated. The last four EADS were expanded 10 times. (*B*) flash photolysis spectroscopy, EADS with time constants indicated. (*C*) species-associated spectra (SAS) from the TA experiments assuming the equilibrium model between P673 and P595 of *SI Appendix*, Fig. S3*A* and Fig. 4, with the species indicated in the panel. The spike feature at 680 nm in P673 results from an artifact. (*D*) SAS of the flash photolysis data.

constants identical to that of the wild type (Fig. 4 and *SI Appendix*, Fig. S3*D*). The resulting SAS are shown in *SI Appendix*, Fig. S4*B*. *SI Appendix*, Fig. S4*C* shows the flash photolysis results, while *SI Appendix*, Fig. S4*D* shows the TA kinetics and the result of the global fit. The SAS were very similar to those of the wild type, indicating that the photocycle dynamics in the PaR1(K332A)R2 mutant are essentially identical to those of the wild type, indicating that the complexity in the dynamics does not result from heterogeneity in the tandem domain.

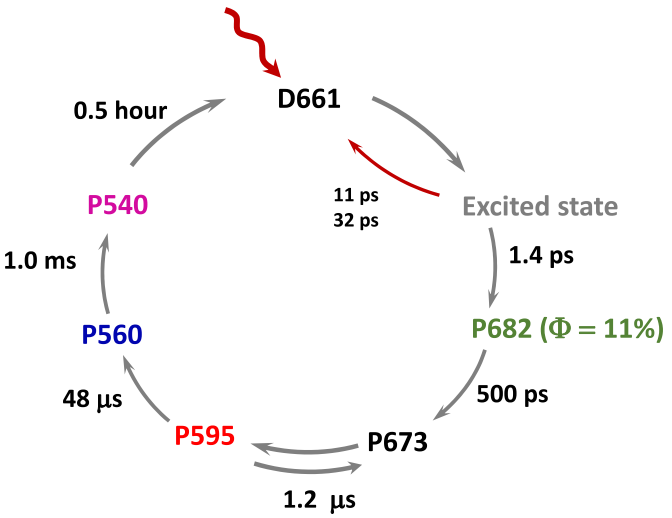

Fig. 4. Bestrhodopsin photocycle upon excitation of the D661 state.

FSRS. To assess the transient structures, in particular the transient isomeric states of the protonated RSB of bestrhodopsin, we studied the D661 reaction dynamics with FSRS on a timescale from fs to sub-ms (26, 33). In the following, we will not consider the FSRS signals of the excited state because they are less informative on the reaction mechanism and because of the full resonance of the Raman pump with the SE (Fig. 3*A*), which may cause artifacts (49). We obtained two datasets for the wild type upon actinic excitation at 650 nm, referred to as dataset I and dataset II, which are characterized by a higher and lower actinic excitation density, respectively. We applied a sequential analysis scheme of which the EADS for dataset II are shown in *SI Appendix*, Fig. S5*B* in the same color coding as for Fig. 3*A* and using the same time constants as for the TA data: 500 ps, 1.2 µs, 48 µs, and an infinite component. *SI Appendix*, Fig. S5*A* shows the FSRS EADS for dataset I using the same time constants and showing very similar spectra but

with a somewhat higher relative amplitude for the last two EADS. Raman difference spectra of product state-minus-dark state are shown, as in our earlier work (26, 29, 33). *SI Appendix*, Fig. S6 shows the raw FSRS kinetics of dataset II at selected wavenumbers, which emphasize the FSRS signals of the photoproducts and the quality of the fit. *SI Appendix*, Fig. S5*C* shows the FSRS data for the Lys mutant using the time constants derived from the TA data. The EADS are very similar to those of the wild type, which again shows that the complexity in the dynamics does not result from heterogeneity in the tandem domain.

Fig. 5 shows the SADS derived from dataset II with the same kinetic model applied to the TA data assuming an equilibrium between P673 and P595. The FSRS signals are dominated by negative contributions due to GSB of the reactant D661 state, with main bands at 952, 1,003, 1,165, and 1,494 cm^{-1}. This observation implies that the combination of Raman cross-section and preresonant enhancement of D661 is larger than that of any of the transient products. To check for consistency between the transient photocycle intermediate P560 that exists on the sub-ms timescale and the Raman spectrum of the photoaccumulated P540 state, in Fig. 5*B*, we first compared the P560 transient FSRS spectrum from dataset I (blue line) and from dataset II (gray line) with the steady-state P540-minus-D661 difference spectrum (red line) that was reconstructed from the data of Fig. 2. Apart from a baseline slowly varying with wavenumber, the spectra are essentially identical with an accurate one-to-one correspondence for each single positive and negative band. The P560 SADS from dataset II (gray line) shows a larger baseline deviation, but the overall bands are at identical positions. This correspondence includes a positive band at 1,218 cm^{-1} that represents the 1,218 cm^{-1} band in the Raman spectrum of the green-absorbing P540 state of Fig. 2 and is indicative of 11-*cis* RSB. We conclude that P560 observed in the transient experiments represents an RSB structure that is essentially identical to that of the P540 state photoaccumulated with red background light and involves RSB in the 11-*cis* isomeric configuration.

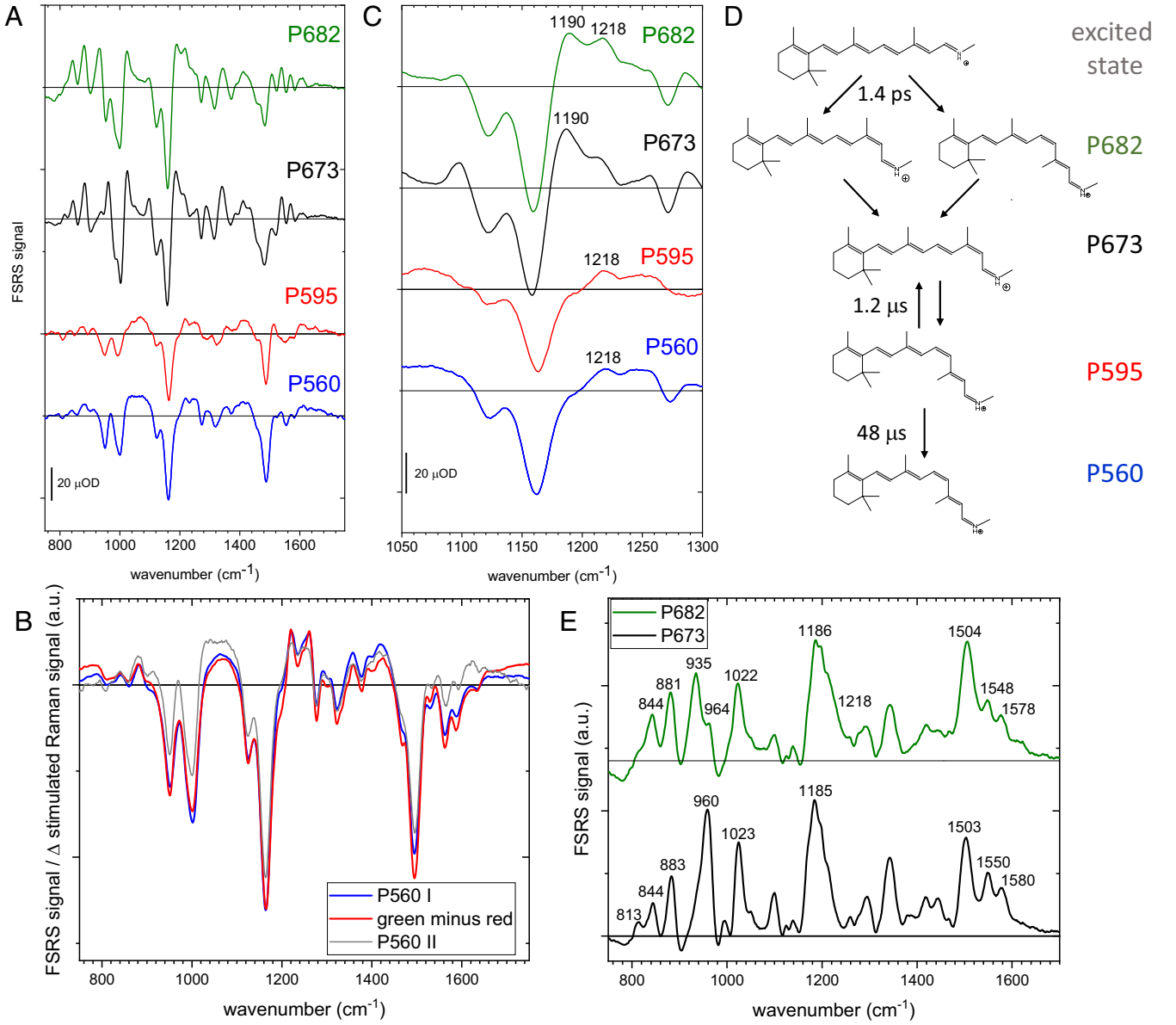

Fig. 5. FSRS of bestrhodopsin. (*A*) FSRS SADS of transient product states; (*B*) transient P560 SADS of dataset I (blue line) and of dataset II (gray line), steady-state green-minus-red stimulated Raman difference spectrum (red line). (*C*) Same as *A* but zoomed in on the fingerprint region. (*D*) RSB isomeric states corresponding to the various intermediates. (*E*) absolute FSRS spectra of P682 and P673 intermediates.

The SADS of the primary photoproduct P682 (Fig. 5 *A* and *C*, green line) has a shape that differs significantly from that of P560, indicating a different RSB structure. It shows the characteristic 1,218 cm^{-1} band like P560, indicative of 11-*cis* RSB. Strikingly, it features a slightly more prominent band at 1,190 cm^{-1}, which is conspicuously absent in the P560 SADS. The 1,190 cm^{-1} C-C fingerprint stretch band corresponds to 13-*cis* retinal (50), as demonstrated for K and K-like intermediates of every microbial rhodopsin studied to date (33, 51–56). Hence, we conclude that P682 likely represents a heterogeneous mixture of 11-*cis* and 13-*cis* RSB. We conclude that from the excited state, all-*trans* RSB may isomerize to both 11-*cis* and 13-*cis* with approximately equal probability, as schematically indicated in Fig. 5*D*. We note that the electronic absorption spectrum of P682 appears to have a sub-structure (Fig. 3*C*, green line), with a pronounced shoulder near 720 nm along with its absorption maximum at 682 nm, which could be the consequence of consisting of two isomeric states.

Next, P682 evolves into P673 in 500 ps. Markedly, the P673 SADS (Fig. 5 *A* and *C*, black line) shows a significantly diminished band at 1,218 cm^{-1} and an increased amplitude at 1,190 cm^{-1} compared to the P682 SADS. This observation strongly suggests that the fraction of 11-*cis* RSB initially formed from the excited state largely converts to 13-*cis* RSB in 500 ps. Hence, P673 likely represents mainly 13-*cis* RSB (Fig. 5*D*), with a possible minor contribution by 11-*cis* RSB.

As demonstrated with TA spectroscopy, in 1.2 µs, the next intermediate P595 (Fig. 5 *A* and *B*, red line) is formed in equilibrium with P673. The P595 FSRS SADS is very similar to that of P560, with a main band at 1,218 cm^{-1} and the absence of a prominent 13-*cis* band at 1,190 cm^{-1}. Hence, we conclude that P595 most likely corresponds to 11-*cis* RSB, and the 1.2 µs equilibration process involves the full conversion of the 13-*cis* RSB to 11-*cis*. Finally, in 48 µs, P595 converts to P560 (Fig. 5 *A* and *B*, blue line), which may be regarded as the stabilized 11-*cis* RSB conformer. *SI Appendix*, Fig. S7 shows the SADS from the equilibrium model for dataset I: overall, the results are similar to those of dataset II, with the exception that the equilibrium model did not result in a perfect separation of P595 and P673 spectral features. The reason for this discrepancy is unclear.

In addition to providing information on the transient isomeric state, the FSRS SADS inform the location and extent of structural deformation of the polyene backbone through the HOOP band frequencies and intensities. P682 and P673 (Fig. 5*A*, green and black lines, respectively) show high intensities of HOOP bands in the 800 to 970 cm^{-1} region, indicative of strong distortions about specific single and double bonds. In contrast, P595 and P560 (Fig. 5*A*, red and blue lines, respectively) show a low HOOP intensity. We conclude that P682 and P673 represent highly distorted 11-*cis* and 13-*cis* RSB conformers, while P595 and P560 are more relaxed 11-*cis* conformers. In Fig. 5*E*, we have reconstructed the absolute FSRS spectra of P682 and P673 by adding appropriate amplitudes of the D661 ground state stimulated Raman spectra. P682 (green line) and P673 (black line) show HOOP amplitudes that are significantly higher than observed in any retinal protein Raman spectrum, including the K and O intermediates of bacteriorhodopsin (37, 57). Assignments of the HOOP modes and other salient modes are given in *SI Appendix, Supporting Text*.

We attempted to decompose the P682 SADS into a superposition of P673 and a separate 11-*cis* fraction. However, this approach was not successful, which implies that the 13-*cis* fraction in P682 undergoes some structural and spectral evolution when converting to P673, the nature of which cannot be determined. We did not succeed in reconstructing the absolute spectra of P595 and P560 due to baseline issues and the lower amplitude of the positive signals with respect to P682 and P673.

The Origin of Multiple Isomerizations in the Early Stages of the Bestrhodopsin Photoreaction. We have demonstrated here that the bestrhodopsin photoreaction involves a multi-step photo-induced isomerization mechanism, where initially a mixture of 11-*cis* and 13-*cis* RSB is formed (together constituting P682) from the all-*trans* excited RSB on the picosecond timescale. Subsequently, the 11-*cis* RSB conformers convert to 13-*cis* in 500 ps to form P673, which, in turn, converts in 1.2 µs to 11-*cis* to form P595 in equilibrium with P673. Hence, extensive isomeric switching occurs on the ground state potential energy surface (PES) after the initial photochemical event that produces P682. The formation of mixed isomeric species with approximately equal occupancy through ultrafast photochemistry and ensuing isomeric switching on the ground state PES observed here is highly unusual, and to the best of our knowledge, has not been observed in any other rhodopsin. In bovine rhodopsin, there is a slight probability of forming 9-*cis* RSB alongside all-trans RSB from the 11-*cis* ground state (1). Photo-induced double isomerizations do occur in other microbial rhodopsins but they were confined to C13=C14, C15=N and are responsible for the light-adaptation of channelrhodopsin (ChR) (58), whereas thermal double isomerization around C13=C14, C15=N occurs during dark adaptation of both bacteriorhodopsin (59) and ChR (58). An ultrafast dual 13 *cis-trans* and 15 *anti-syn* isomerization was proposed for an ultraviolet-absorbing rhodopsin (26), but these occur in parallel and not sequentially as we have observed here.

In bacteriorhodopsin, the all-*trans* to 13-*cis* isomerization involves an aborted bicycle-pedal isomerization of (mainly) the C11 = C12 — C13 = C14 bonds (23, 24, 60, 61). The bicycle pedal mechanism implies that the C11=C12 and C13=C14 double bonds co-rotate in opposite directions in the excited state so as to conserve volume (62), as indicated in Fig. 6*A*: in bacteriorhodopsin, the C11=C12 rotation is aborted while the system proceeds through the conical intersection at the C13=C14 reaction coordinate, resulting in 13-*cis* RSB. The energy content of the bacteriorhodopsin K intermediate is about 10 kCal/mole (63, 64), which corresponds to about 20% of the initial photon energy. The conical intersection was estimated to lie at 30 kCal/mole (60), implying that the system energetically relaxes by 20 kCal/mole after passing through the CI. This energy difference is >30 times the thermal energy at ambient temperature, which explains why K is stable at 13-*cis* in bacteriorhodopsin. The relaxation is due to the release of structural strain in the RSB: after passing through the CI, the RSB is highly twisted about many bonds (which is a feature of the aborted bicycle-pedal isomerization), and after relaxation to K, the C13=C14 bond attains a dihedral angle of 160°, which is close to planarity at 180°. From such a state, the RSB could never change its isomeric state on fast timescales.

In bestrhodopsin, the situation is quite different from bacteriorhodopsin but may be understood by considering the fundamental properties of the bacteriorhodopsin isomerization mechanism and the current FSRS results. A key feature of the bestrhodopsin photoreaction is that 11-*cis* and 13-*cis* RSB are initially formed, and these two species are subsequently kinetically connected (i.e., they interconvert) on the 500 ps to µs timescales. Our results on the Lys mutant demonstrate that these features are inherent to single rhodopsin domains and do not follow from heterogeneity in the tandem domain. These observations demonstrate that two conical intersections must be present on the excited-state PES, with one that leads to 11-*cis* RSB

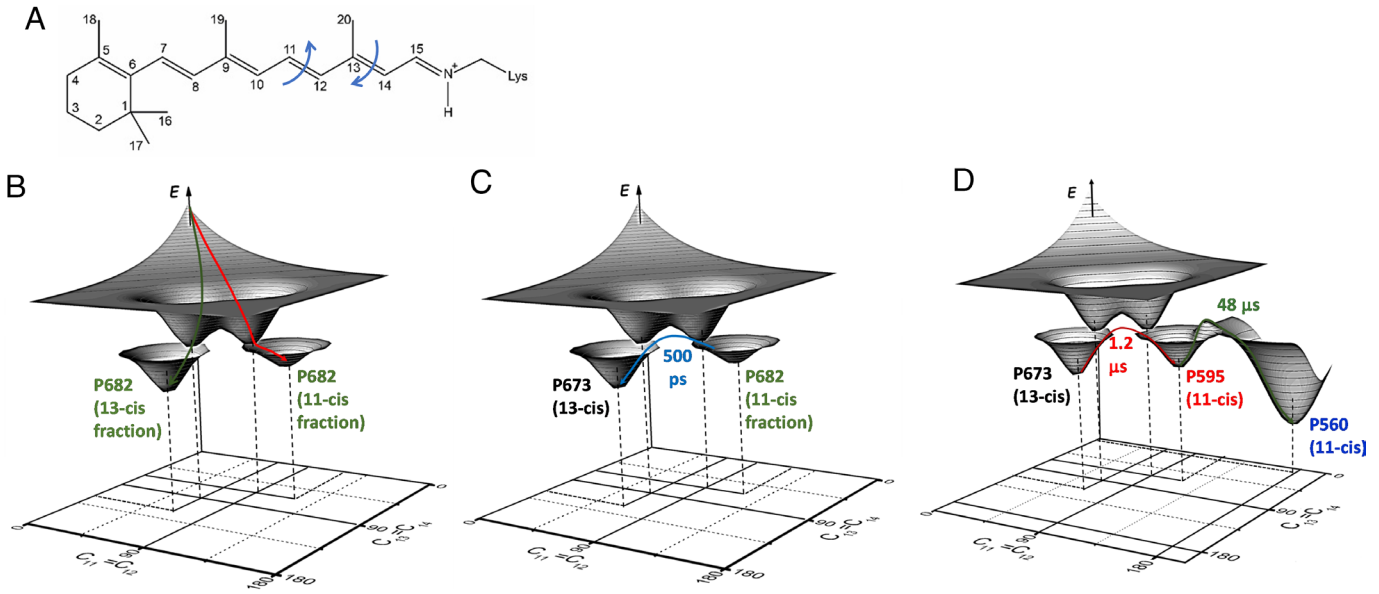

Fig. 6. Isomerization pathways and PESs of bestrhodopsin. (*A*) rotations about the C11=C12 and C13=C14 double bonds in the bicycle-pedal isomerization mechanism; (*B*) schematic PES for bestrhodopsin, branching of excited states into the conical intersection to 11-*cis* (red pathway) and 13-*cis* (green pathway) via aborted bicycle pedal mechanisms to form P682, which consists of a mixture of 11-*cis* and 13-*cis* conformers. After passing through either CI, RSB becomes structurally trapped close to the conical intersections high up on the ground state PES. (*C*) same as *B*, with the 11-*cis* RSB fraction of P682 converting to 13-*cis* RSB on the ground state PES within 500 ps to form P673 (blue pathway). (*D*) same as *B* and *C*, with an energetic lowering of the initially populated 11-*cis* potential energy well. As a result, the 13-*cis* population of P673 converts to 11-*cis* of P595 in 1.2 µs in equilibrium (red pathway). Subsequently, P595 evolves to P560 in 48 µs (green pathway). The C11=C12 and C13=C14 angles are indicative and by no means quantitative.

(Fig. 6*A*, red trajectory) and one that leads to 13-*cis* RSB (Fig. 6*A*, green trajectory), branching off from the initially populated Franck–Condon region. We propose that an aborted bicycle pedal motion occurs in both cases with co-rotation of C11=C12 and C13=C14 in opposing directions, similar to bacteriorhodopsin. However, in a fraction of the reactive RSBs in bestrhodopsin, C11=C12 rotation is not aborted. Instead, the C13=C14 rotation is aborted to result in passing through the C11=C12 conical intersection, forming 11-*cis* RSB. This pathway may be promoted by the significant initial twist of RSB at the C11=C12 *trans* bond in the D661 dark state. Judging from the notably high amplitude HOOP mode at 952 cm^{-1} (Fig. 2, red line), this HOOP has a significantly higher amplitude than those found for light-adapted bacteriorhodopsin (38), indicating a significant initial twist angle. In parallel, in the other reactive RSB fraction, a reaction similar to bacteriorhodopsin takes place with an abortion of the C11=C12 rotation but not of the C13=C14 rotation, and the system passes through the C13=C14 conical intersection to form a fraction of 13-*cis* RSB. Fig. 6*A* schematically sketches this situation. The RSB binding pocket may be structurally attuned to (transiently) accommodate 11-*cis* as well as 13-*cis* RSB, in contrast to other microbial rhodopsins.

For simplicity, the trajectories to the two different CIs in Fig. 6*A* are drawn as barrierless, yet the system very likely needs to cross a barrier on the excited state PES before reaching the CIs given the relatively long excited-state lifetime of 1.4 ps. Hence, we propose that the system dwells on the excited-state PES for 1.4 ps facing a barrier, and once crossing the barrier from that point evolves to the two different CIs, which occurs on a much faster timescale. The latter process cannot be resolved with time-resolved spectroscopy methods because these intermediates do not transiently accumulate. Our results furthermore indicate that the concomitant formation 11-*cis* and 13-*cis* RSB in P682 does not result from a ground-state heterogeneity in the R2 rhodopsin domain: the 11-*cis* and 13-*cis* potential energy wells must be connected on the same PES and hence must feature two CIs, otherwise isomeric switching in 500 ps and 1.2 µs on the ground state PES could never take place. We note that the J intermediate of bacteriorhodopsin, which precedes K on the ps timescale, does not resemble P673, where J is a vibrationally excited, structurally similar form of K that highly evolved along the C13=C14 reaction coordinate and not anywhere close to the CI (57).

After having passed through either of the conical intersections and residing on the ground state PES in either 13-*cis* or 11-*cis* RSB, these two states must be energetically and conformationally close in order to allow the 11-*cis* to 13-*cis* conversion to happen in 500 ps (P682 to P673 evolution) and the ensuing 13-*cis* to 11-*cis* conversion in 1.2 µs (P673 to P595 evolution). We now recall that the HOOP intensities of P682 and P673 are significantly larger than in canonical primary intermediates, such as K in bacteriorhodopsin (57), which indicates that a large amount of free energy is stored as RSB strain in bestrhodopsin. The RSB does not structurally relax but stays energetically close to either of the CIs after passing through it, with the dihedral angles that constitute the aborted bicycle pedal motion progressing not far beyond the points defined by the CIs. We presume that a structural conflict of isomerized RSB with amino acid side chains in the RSB binding pocket may be responsible for such arrested motions. Because of the similar volume-conserving bicycle pedal motions resulting in 11-*cis* and 13-*cis* in P682, the condition stated at the top of this paragraph will be met, i.e., these two states will indeed lie energetically and conformationally close together on the ground state PES, as indicated in Fig. 6*B*. This allows the thermal conversion of P682 to P673 in 500 ps, involving conversion of the 11-*cis* fraction of P682 to 13-*cis* RSB, where the latter is apparently lower in energy than the former (Fig. 6*C*). For this structural conversion from 11-*cis* to 13-*cis* to occur, the C11=C12 and C13=C14 dihedral angles need to rotate in concert only by possibly a few tens of degrees, passing over a relatively low energy barrier on the ground state PES (Fig. 6*C*, blue trajectory). In addition, a minor

spectral and structural relaxation of the 13-*cis* fraction of P682 likely takes place, which has not been indicated in the figure.

After converting from 11-*cis* to 13-*cis* in 500 ps (the P682 to P673 conversion), RSB fully converts to 11-*cis* in 1.2 μs (P682 to P595 conversion, in equilibrium), as schematically indicated in Fig. 6*D*. While 11-*cis* RSB in P682 must be energetically higher than 13-*cis* RSB in P673, given the unidirectional population transfer in 500 ps, 11-*cis* RSB in P595 must be energetically similar to P673 in order to establish a thermal equilibrium. Hence, the 11-*cis* potential energy well has lowered. Indeed, the HOOP intensity of P595 is much lower than that of P673 and P682, indicating that the RSB strain has been significantly released, lowering its free energy. We presume that in P595 a protein structural change has occurred in the RSB binding pocket that is more accommodating to 11-*cis* RSB, allowing it to structurally relax. A part of the free energy may have been transferred to the protein as structural strain, which may explain why P595 is energetically similar to P673 (which has a highly strained RSB chromophore). Fig. 6*D* sketches the conversion from 13-*cis* RSB to 11-*cis* RSB in 1.2 μs over a low energy barrier on the ground state PES (red curve). Finally, the strain in the RSB and protein is relaxed in 48 μs (Fig. 6*D*, green curve), reaching the nearly meta-stable state P560, which then undergoes a minor relaxation to the meta-stable state P540 (not indicated in Fig. 6*D*).

Concluding Remarks

Bestrhodopsin shows previously unobserved isomerization dynamics that involve a surprisingly complex sequence of events that comprise back-and-forth switching between 11-*cis* and 13-*cis* RSB on multiple timescales. We find that the RSB binding pocket is conducive for all-*trans* to 13-*cis* photoisomerization as well as all-*trans* to 11-*cis* photoisomerization, which we described as excited RSB branching off from the Franck–Condon region to follow two separate paths through two distinct CIs. It is unclear which factors cause the isomerization pathway to 11-*cis* RSB to exist alongside the canonical reaction path to 13-*cis* RSB. First, the RSB binding pocket is likely structurally different from canonical microbial rhodopsins and (transiently) accommodating for 11-*cis* as well as 13-*cis* RSB. Second, the significant pre-twist of the C11=C12 double bond in the D661 state may constitute an important determinant. Third, static or dynamic heterogeneity may underlie this phenomenology: Dynamically interconverting conformational microstates (48) may feature particular shapes of the excited-state PES and determine whether the initial isomerization trajectory results in 11-*cis* or 13-*cis* RSB. Fourth, a red-shifted absorption spectrum may result in destabilization of the 13-*cis* isomerization reaction coordinate (13, 65), rendering the 11-*cis* pathway more favorable in relative terms. Regardless, any initially formed 11-*cis* RSB is forced to convert to 13-*cis* on the 500 ps timescale, likely as a result of possibly dynamic steric constraints imposed by the RSB binding pocket, irrespective of the protein conformational microstate at hand.

In protonated all-*trans* RSB in an organic solution, a mixture of 9-*cis*, 11-*cis*, and 13-*cis* isomers were observed upon irradiation (66) which is reminiscent of the situation in bestrhodopsin. However, different from the situation in organic solvent that provides a high degree of conformational flexibility, the 11-*cis* and 13-*cis* RSB in the P682 and P673 intermediates of bestrhodopsin are highly strained, implying that the RSB binding pocket causes significant steric conflicts upon isomerization that ultimately define the photochemical outcome. Indeed, molecular dynamics simulations on bacteriorhodopsin suggested that steric conflicts in the RSB binding pocket prevent photoisomerization paths other than toward 13-*cis* (67).

FSRS studies on bestrhodopsin open a unique window in our understanding of rhodopsin photodynamics by revealing structural intermediates that exist immediately after passing through the CI. These structurally sensitive experiments provide a rare opportunity to study highly distorted and reactive intermediates in great detail in the solution phase at physiological temperature. In canonical microbial rhodopsins such as bacteriorhodopsin, such states do not transiently accumulate and instead rapidly evolve to structurally relaxed J and K-like intermediates, in the solution phase as well as in crystals (56, 57, 68). Overall, the complex chromophore isomerization dynamics on the ground state PES in bestrhodopsin are likely due to a changing potential energy landscape that certainly must be associated with structural changes in the protein, as the timescale, specificity, and directionality indicate that this is not a stochastic switching between conformations. Here, computational modeling and molecular dynamics simulations of the entire pigment- protein system on extended timescales may provide valuable insights (69).

Methods

Methods are described in *SI Appendix*.

Data, Materials, and Software Availability. The research data have been deposited at DataverseNL, Kennis, John, Research data for multiple retinal isomerizations during the early phase of the bestrhodopsin photoreaction, https://doi.org/10.34894/TXUZJX (70).

ACKNOWLEDGMENTS. We are grateful to Massimo Olivucci (University of Siena/Bowling Green), Igor Schapiro (Hebrew University of Jerusalem), and Tomotsumi Fujisawa (Saga University) for insightful discussions. M.B., P.H., and J.T.M.K. acknowledge beam time access at ELI. The work is supported by the German Research Foundation (DFG, grant 509731234, M.B.), the European Research Council (Synergy "SOL" 951644, P.H.), and the Czech Science Foundation (project No. 21-09692M). P.H. is a Hertie Professor and is supported by the Hertie Foundation.

1. O. P. Ernst *et al.*, Microbial and animal rhodopsins: Structures, functions, and molecular mechanisms. *Chem. Rev.* **114**, 126–163 (2014).
2. E. G. Govorunova, O. A. Sineshchekov, H. Li, J. L. Spudich "Microbial rhodopsins: Diversity, mechanisms, and optogenetic applications" in *Annual Review of Biochemistry*, R. D. Kornberg, Ed. (Annual Reviews, 2017), vol. 86, pp. 845–872.
3. F. Zhang *et al.*, The microbial opsin family of optogenetic tools. *Cell* **147**, 1446–1457 (2011).
4. D. R. Hochbaum *et al.*, All-optical electrophysiology in mammalian neurons using engineered microbial rhodopsins. *Nat. Methods* **11**, 825–833 (2014).
5. M. Luck *et al.*, A photochromic histidine kinase rhodopsin (HKR1) that is bimodally switched by ultraviolet and blue light. *J. Biol. Chem.* **287**, 40083-90 (2012).
6. S. Mukherjee, P. Hegemann, M. Broser, Enzymerhodopsins: Novel photoregulated catalysts for optogenetics. *Curr. Opin. Struct. Biol.* **57**, 118–126 (2019).
7. A. Rozenberg *et al.*, Rhodopsin-bestrophin fusion proteins from unicellular algae form gigantic pentameric ion channels. *Nat. Struct. Mol. Biol.* **29**, 592–603 (2022).
8. A. Herdean *et al.*, A voltage-dependent chloride channel fine-tunes photosynthesis in plants. *Nat. Commun.* **7**, 11654 (2016).
9. L. T. Chien, Z. R. Zhang, H. C. Hartzell, Single Cl- channels activated by Ca2+ in Drosophila S2 cells are mediated by bestrophins. *J. Gen. Physiol.* **128**, 247–259 (2006).
10. A. Mukherjee *et al.*, Thylakoid localized bestrophin-like proteins are essential for the CO2 concentrating mechanism of Chlamydomonas reinhardtii. *Proc. Natl. Acad. Sci. U.S.A.* **116**, 16915–16920 (2019).
11. A. Burlacot *et al.*, Alternative photosynthesis pathways drive the algal CO2-concentrating mechanism. *Nature* **605**, 366–371 (2022).
12. M. Broser *et al.*, NeoR, a near-infrared absorbing rhodopsin. *Nat. Commun.* **11**, 5682 (2020).
13. M. Broser *et al.*, Experimental assessment of the electronic and geometrical structure of a near-infrared absorbing and highly fluorescent microbial rhodopsin. *J. Phys. Chem. Lett.* **14**, 9291–9295 (2023).
14. M. Sugiura *et al.*, Unusual photoisomerization pathway in a near-infrared light absorbing enzymerhodopsin. *J. Phys. Chem. Lett.* **13**, 9539–9543 (2022).
15. K. Oda *et al.*, Crystal structure of the red light-activated channelrhodopsin Chrimson. *Nat. Commun.* **9**, 3949 (2018).

16. D. Urmann *et al.*, Photochemical properties of the red-shifted channelrhodopsin chrimson. *Photochem. Photobiol.* **93**, 782–795 (2017).
17. R. Weissleder, V. Ntziachristos, Shedding light onto live molecular targets. *Nat. Med.* **9**, 123–128 (2003).
18. J. Vierock *et al.*, BiPOLES is an optogenetic tool developed for bidirectional dual-color control of neurons. *Nat. Commun.* **12**, 4527 (2021).
19. J. A. Strother *et al.*, The emergence of directional selectivity in the visual motion pathway of Drosophila. *Neuron* **94**, 168–182.e10 (2017).
20. M. Braiman, R. Mathies, Resonance raman evidence for an all-trans to 13-cis isomerization in the proton-pumping cycle of bacteriorhodopsin. *Biochemistry* **19**, 5421–5428 (1980).
21. M. Braiman, R. Mathies, Resonance raman-spectra of bacteriorhodopsins primary photoproduct–Evidence for a distorted 13-cis retinal chromophore. *Proc. Natl. Acad. Sci. U.S.A.* **79**, 403–407 (1982).
22. K. Edman *et al.*, High-resolution X-ray structure of an early intermediate in the bacteriorhodopsin photocycle. *Nature* **401**, 822–826 (1999).
23. P. Nogly *et al.*, Retinal isomerization in bacteriorhodopsin captured by a femtosecond x-ray laser. *Science* **361**, eaat0094 (2018).
24. G. N. Kovacs *et al.*, Three-dimensional view of ultrafast dynamics in photoexcited bacteriorhodopsin. *Nat. Commun.* **10**, 3177 (2019).
25. P. Kukura, D. W. McCamant, R. A. Mathies, Femtosecond stimulated Raman spectroscopy. *Ann. Rev. Phys. Chem.* **58**, 461–488 (2007).
26. Y. Hontani *et al.*, Dual photoisomerization on distinct potential energy surfaces in a UV-absorbing rhodopsin. *J. Am. Chem. Soc.* **142**, 11464–11473 (2020).
27. P. C. Andrikopoulos *et al.*, Femtosecond-to-nanosecond dynamics of flavin mononucleotide monitored by stimulated Raman spectroscopy and simulations. *Phys. Chem. Chem. Phys.* **22**, 6538–6552 (2020).
28. Y. Hontani *et al.*, Molecular origin of photoprotection in Cyanobacteria probed by watermarked femtosecond stimulated raman spectroscopy. *J. Phys. Chem. Lett.* **9**, 1788–1792 (2018).
29. M. Kloz, J. Weissenborn, T. Polivka, H. A. Frank, J. T. M. Kennis, Spectral watermarking in femtosecond stimulated Raman spectroscopy: Resolving the nature of the carotenoid S-star state. *Phys. Chem. Chem. Phys.* **18**, 14619–14628 (2016).
30. J. M. A. Vivancos *et al.*, Unraveling the excited-state dynamics and light-harvesting functions of Xanthophylls in light-harvesting complex II using femtosecond stimulated raman spectroscopy. *J. Am. Chem. Soc.* **142**, 17346–17355 (2020).
31. Y. Hontani *et al.*, The femtosecond-to-second photochemistry of red-shifted fast-closing anion channelrhodopsin PsACR1. *Phys. Chem. Chem. Phys.* **19**, 30402–30409 (2017).
32. Y. Hontani *et al.*, Reaction dynamics of the chimeric channelrhodopsin C1C2. *Sci. Rep.* **7**, 7217 (2017).
33. Y. Hontani *et al.*, The photochemistry of sodium ion pump rhodopsin observed by watermarked femto- to submillisecond stimulated Raman spectroscopy. *Phys. Chem. Chem. Phys.* **18**, 24729–24736 (2016).
34. Y. Hontani *et al.*, Strong pH-dependent near-infrared fluorescence in a microbial rhodopsin reconstituted with a red-shifting retinal analogue. *J. Phys. Chem. Lett.* **9**, 6469–6474 (2018).
35. Y. Hontani *et al.*, Real-time observation of tetrapyrrole binding to an engineered bacterial phytochrome. *Commun. Chem.* **4**, 3 (2021).
36. K. Kajimoto *et al.*, Transient resonance raman spectroscopy of a light-driven sodium-ion-pump rhodopsin from indibacter alkaliphilus. *J. Phys. Chem. B* **121**, 4431–4437 (2017).
37. S. O. Smith *et al.*, Chromophore structure in bacteriorhodopsins-o640 photointermediate. *Biochemistry* **22**, 6141–6148 (1983).
38. S. O. Smith *et al.*, Vibrational analysis of the all-trans-retinal chromophore in light-adapted bacteriorhodopsin. *J. Am. Chem. Soc.* **109**, 3108–3125 (1987).
39. B. Curry, A. Broek, J. Lugtenburg, R. Mathies, Vibrational analysis of all-trans-retinal. *J. Am. Chem. Soc.* **104**, 5274–5286 (1982).
40. G. Eyring, B. Curry, A. Broek, J. Lugtenburg, R. Mathies, Assignment and interpretation of hydrogen out-of-plane vibrations in the resonance raman-spectra of rhodopsin and bathorhodopsin. *Biochemistry* **21**, 384–393 (1982).
41. R. Berera, R. van Grondelle, J. T. M. Kennis, Ultrafast transient absorption spectroscopy: Principles and application to photosynthetic systems. *Photosynthesis Res.* **101**, 105–118 (2009).
42. I. H. M. van Stokkum, D. S. Larsen, R. van Grondelle, Global and target analysis of time-resolved spectra. *Biochim. Biophys. Acta* **1657**, 82–104 (2004).
43. J. T. M. Kennis *et al.*, Ultrafast protein dynamics of bacteriorhodopsin probed by photon echo and transient absorption spectroscopy. *J. Phys. Chem. B* **106**, 6067–6080 (2002).
44. I. H. M. van Stokkum *et al.*, (Sub)-picosecond spectral evolution of fluorescence in photoactive proteins studied with a synchroscan streak camera system. *Photochem. Photobiol.* **82**, 380–388 (2006).
45. S. Rouhani *et al.*, Crystal structure of the D85S mutant of bacteriorhodopsin: Model of an O-like photocycle intermediate. *J. Mol. Biol.* **313**, 615–628 (2001).
46. M. O. Lenz, A. C. Woerner, C. Glaubitz, J. Wachtveitl, Photoisomerization in proteorhodopsin mutant D97N. *Photochem. Photobiol.* **83**, 226–231 (2007).
47. F. Scholz, E. Bamberg, C. Bamann, J. Wachtveitl, Tuning the primary reaction of channelrhodopsin-2 by imidazole, pH, and site-specific mutations. *Biophys. J.* **102**, 2649–2657 (2012).
48. I. H. M. Van Stokkum *et al.*, Reaction dynamics in the chrimson channelrhodopsin: Observation of product-state evolution and slow diffusive protein motions. *J. Phys. Chem. Lett.* **14**, 1485–1493 (2023).
49. D. W. McCamant, P. Kukura, R. A. Mathies, Femtosecond stimulated Raman study of excited-state evolution in bacteriorhodopsin. *J. Phys. Chem. B* **109**, 10449–10457 (2005).
50. S. O. Smith, J. A. Pardoen, J. Lugtenburg, R. A. Mathies, Vibrational analysis of the 13-cis-retinal chromophore in dark-adapted bacteriorhodopsin. *J. Phys. Chem.* **91**, 804–819 (1987).
51. A. Yi *et al.*, Structural changes in an anion channelrhodopsin: Formation of the K and L Intermediates at 80 K. *Biochemistry* **56**, 2197–2208 (2017).
52. J. I. Ogren *et al.*, Comparison of the structural changes occurring during the primary phototransition of two different channelrhodopsins from Chlamydomonas Algae. *Biochemistry* **54**, 377–388 (2015).
53. Y. Nakamizo *et al.*, Low-temperature Raman spectroscopy of sodium-pump rhodopsin from Indibacter alkaliphilus: Insight of Na+ binding for active Na+ transport. *Phys. Chem. Chem. Phys.* **23**, 2072–2079 (2021).
54. T. Fujisawa, H. Kiyota, T. Kikukawa, M. Unno, Low-temperature raman spectroscopy of halorhodopsin from natronomonas pharaonis: Structural discrimination of blue-shifted and red-shifted photoproducts. *Biochemistry* **58**, 4159–4167 (2019).
55. T. Fujisawa *et al.*, Low-temperature Raman spectroscopy reveals small chromophore distortion in primary photointermediate of proteorhodopsin. *Febs Lett.* **592**, 3054–3061 (2018).
56. J. Herbst, K. Heyne, R. Diller, Femtosecond infrared spectroscopy of bacteriorhodopsin chromophore isomerization. *Science* **297**, 822–825 (2002).
57. S. Shim, J. Dasgupta, R. A. Mathies, Femtosecond time-resolved stimulated raman reveals the birth of bacteriorhodopsin's J and K intermediates. *J. Am. Chem. Soc.* **131**, 7592–7597 (2009).
58. J. Kuhne *et al.*, Unifying photocycle model for light adaptation and temporal evolution of cation conductance in channelrhodopsin-2. *Proc. Natl. Acad. Sci. U.S.A.* **116**, 9380–9389 (2019).
59. A. Wand, N. Friedman, M. Sheves, S. Ruhman, Ultrafast photochemistry of light-adapted and dark-adapted bacteriorhodopsin: Effects of the initial retinal configuration. *J. Phys. Chem. B* **116**, 10444–10452 (2012).
60. P. Altoe, A. Cembran, M. Olivucci, M. Garavelli, Aborted double bicycle-pedal isomerization with hydrogen bond breaking is the primary event of bacteriorhodopsin proton pumping. *Proc. Natl. Acad. Sci. U.S.A.* **107**, 20172–20177 (2010).
61. S. Gozem, H. L. Luk, I. Schapiro, M. Olivucci, Theory and simulation of the ultrafast double-bond Isomerization of biological chromophores. *Chem. Rev.* **117**, 13502–13565 (2017).
62. S. Sen, R. K. Kar, V. A. Borin, I. Schapiro, Insight into the isomerization mechanism of retinal proteins from hybrid quantum mechanics/molecular mechanics simulations. *Wiley Interdisc. Rev. Comput. Mol. Sci.* **12**, e1562 (2022).
63. S. L. Logunov, M. A. ElSayed, Redetermination of the quantum yield of photoisomerization and energy content in the K–intermediate of bacteriorhodopsin photocycle and its mutants by the photoacoustic technique. *J. Phys. Chem. B* **101**, 6629–6633 (1997).
64. R. R. Birge *et al.*, Revised assignment of energy-storage in the primary photochemical event in bacteriorhodopsin. *J. Am. Chem. Soc.* **113**, 4327–4328 (1991).
65. L. Barneschi *et al.*, On the fluorescence enhancement of arch neuronal optogenetic reporters. *Nat. Commun.* **13**, 6432 (2022).
66. K. A. Freedman, R. S. Becker, Comparative investigation of the photoisomerization of the protonated and unprotonated normal-butylamine schiff-bases of 9-cis-retinals, 11-cis-retinals, 13-cis-retinals. and all-trans-retinals. *J. Am. Chem. Soc.* **108**, 1245–1251 (1986).
67. S. Hayashi, E. Tajkhorshid, K. Schulten, Molecular dynamics simulation of bacteriorhodopsin's photoisomerization using ab initio forces for the excited chromophore. *Biophys. J.* **85**, 1440–1449 (2003).
68. Z. Ren, Photoinduced isomerization sampling of retinal in bacteriorhodopsin. *PNAS Nexus* **1**, pgac103 (2022).
69. L. Pedraza-González, E. Cignoni, J. D'Ascenzi, L. Cupellini, B. Mennucci, How the pH controls photoprotection in the light-harvesting complex of mosses. *J. Am. Chem. Soc.* **145**, 7482–7494 (2023).
70. J. T. M. Kennis, Multiple Retinal Isomerizations during the Early Phase of the Bestrhodopsin Photoreaction. Research Data. https://doi.org/10.34894/TXUZJX. Deposited 26 February 2024.